Ring-Resonator-Based Coupling Architecture for Enhanced Connectivity in a Superconducting Multiqubit Network

Sumeru Hazra, Anirban Bhattacharjee, Madhavi Chand, Kishor V. Salunkhe, Sriram Gopalakrishnan,[†] Meghan P. Patankar, and R. Vijay[*]

Department of Condensed Matter Physics and Materials Science, Tata Institute of Fundamental Research, 1 Homi Bhabha Road, Mumbai 400005, India

(Received 3 November 2020; revised 15 July 2021; accepted 19 July 2021; published 11 August 2021)

Qubit coherence and gate fidelity are typically considered the two most useful metrics for characterizing a quantum processor. An equally useful metric is interqubit connectivity as it minimizes gate count and allows implementing algorithms efficiently with reduced error. However, interqubit connectivity in superconducting processors tends to be limited to nearest neighbor due to practical constraints in typical planar realizations. Here, we introduce a superconducting architecture that uses a ring resonator as a multiqubit coupling element to provide beyond nearest-neighbor connectivity without compromising on coupling uniformity or introducing fabrication complexities. We theoretically analyze the interqubit coupling as a function of frequency for a pair of qubits placed at different positions along the ring resonator and show that for carefully chosen operating frequency and angular spacing between the qubits, the variation of coupling can be minimized. For an operating frequency between the first two resonances of the ring resonator and a 30° angular spacing for qubits, we compute interqubit coupling for a device capable of supporting up to 12 qubits with each qubit connected to nine other qubits. Using four qubits positioned strategically in the ring-resonator coupler, we experimentally verify the theoretical prediction for all possible angular spacings between the two qubits and demonstrate good agreement. Just like the standard bus resonator coupler, the coupling in the ring-resonator coupler is mediated via virtual photons since the operating frequency is far away from the resonant modes of the ring coupler. This ensures that any small internal loss in the ring resonator does not introduce decoherence during the coupling operation. We also compute extensions of this idea involving larger ring resonators and a multiring system and show the possibility of highly connected networks with larger number of qubits. Apart from being plug and play for existing superconducting architectures, our concept is scalable, adaptable to other platforms and has the potential to significantly accelerate progress in quantum computing, annealing, simulations, and error correction.

DOI: 10.1103/PhysRevApplied.16.024018

I. INTRODUCTION

Quantum-information processors promise tremendous computational advantages in solving a broad class of problems, offering polynomial [1] and even sometimes exponential [2] speed ups compared to the best-known implementation in classical computers. Continual efforts across several platforms have propelled the field from proof-of-concept demonstrations with a few qubits to actual processors with tens of qubits [3–6], leading to the recent milestone of achieving quantum supremacy [7]. Quantum algorithms generally assume the ability to implement gates between any arbitrary pair of qubits in a processor. However, it is often impractical or topologically impossible to engineer a processor with arbitrarily long-range coupling. Therefore, in order to implement an arbitrary quantum operation in such a constrained architecture, the quantum data needs to be transported across several connected qubits in the grid, leading to additional operations and consequently more errors. More recently, the relevance of qubit connectivity for quantum annealers [8] and the performance of near-term quantum processors as quantified by the quantum volume metric [9] have also been studied.

Among the two leading platforms for a practical quantum processor, all-to-all connectivity has been demonstrated in the ion-trap system for up to 11 qubits [10], whereas even the most powerful superconducting processors today provide only nearest-neighbor connectivity achieved by direct capacitive coupling [11], tunable couplers [12] or bus resonators [13]. Figure 1(a) shows a typical planar layout of qubits connected by bus resonators. While recent experiments [5,14] have implemented all-to-all connectivity by using a single bus

[*]Corresponding author. r.vijay@tifr.res.in

[†]Present address: Institute of Quantum Computing, University of Waterloo, Waterloo, Ontario N2L 3G1, Canada.

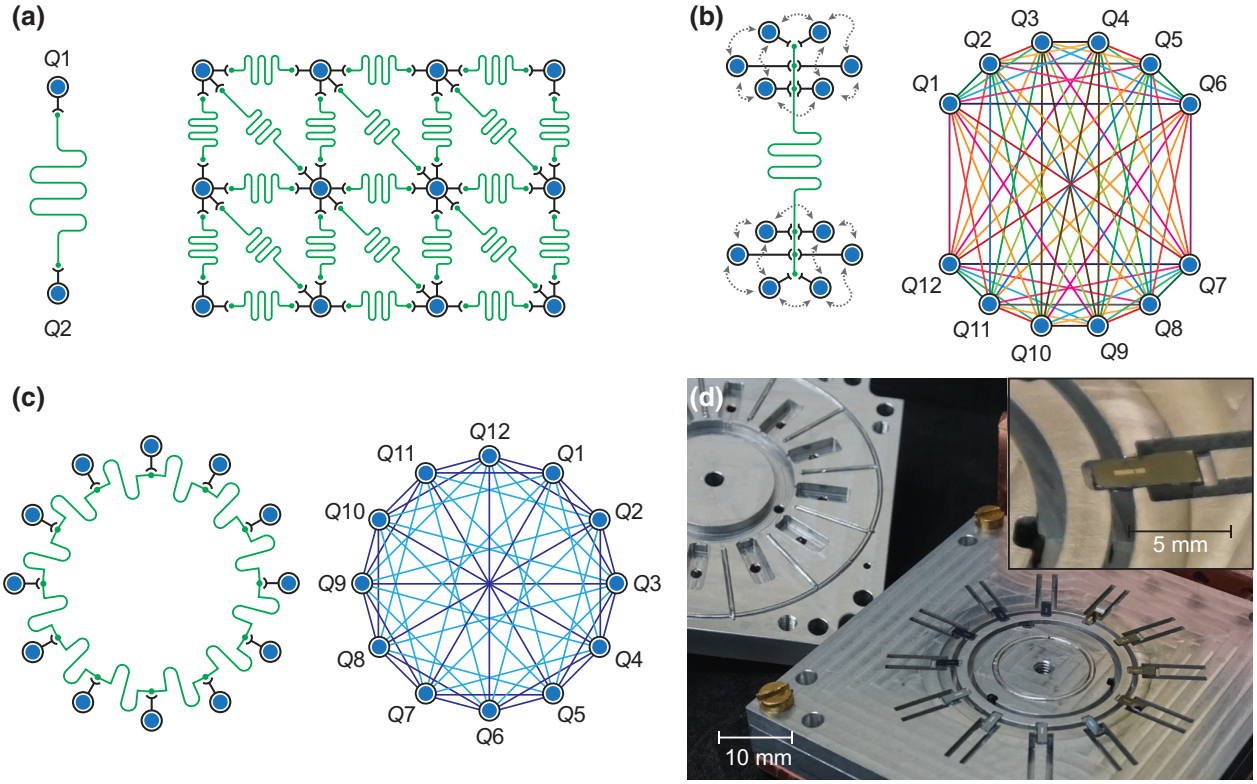

FIG. 1. Interqubit connectivity in superconducting circuit architecture. (a) A standard bus resonator connecting two qubits positioned at its antinodes. Extension to a two-dimensional (2D) grid layout, which achieves uniform but only nearest-neighbor coupling. (b) Several qubits placed in close proximity at each antinode of a bus resonator produces all-to-all connectivity. However, one typically observes wide variation in interqubit coupling and unwanted crosstalk (gray dashed arrows) (c) Our design uses a ring resonator as a multipath coupling element connecting several qubits. It offers a highly connected scalable qubit network with only two slightly different values for interqubit coupling with negligible crosstalk. (d) Image of a semiassembled three-dimensional (3D) circuit quantum electrodynamics (cQED) implementation of a 12-qubit network. The qubit slots (magnified in the inset) are placed 30° apart and the readout resonators are $\lambda/4$ sections of transmission line extending radially outward.

resonator with many superconducting qubits connected at its antinodes [Fig. 1(b)], the interqubit coupling strength varies significantly from pair to pair and the close proximity of qubits leads to unwanted crosstalk. In this paper, we propose an alternative scalable architecture for a network of superconducting qubits with significantly enhanced interqubit connectivity. The key idea in this architecture is the use of a ring resonator as a bus resonator capable of mediating interaction between several qubits. As shown in Fig. 1(c), the qubits are distributed throughout the circumference of the ring resonator and thus spatially separated. This provides good microwave isolation resulting in individual qubit addressability and negligible qubit crosstalk [14]. By choosing the angular spacing and operating frequency carefully, one can achieve high connectivity while minimizing variation in interqubit coupling for different qubit pairs. An example with 12 qubits where each qubit is connected to nine other qubits is illustrated in Fig. 1(c). The architecture proposed here is completely agnostic to the kind of two-qubit gates to be implemented and is compatible with both flux-activated gates using tunable qubits [11,15–18] and microwave-drive-activated gates using fixed frequency qubits [19,20] offering wide compatibility. Further, this idea can be extended to other architectures, which rely on bus cavities for coupling [21,22].

II. RING RESONATOR COUPLER: THEORY

Ring resonators are an example of distributed element resonators with periodic boundary conditions and have been widely used in optical systems [23]. Often known as whispering-gallery-mode resonators, they have been recently used in superconducting quantum circuits as well for building high-Q resonators [24]. For a perfectly symmetric ring resonator, a characteristic feature is the uniform standing-wave amplitude independent of the position along the resonator. This would mean that the qubit-resonator coupling is independent of its position in the ring resonator. However, from the perspective of using such a system as a coupler, this does not ensure an interqubit coupling independent of relative qubit position

[25]. Resonator-based couplers operate detuned from the qubit transitions [13] in order to be insensitive to losses in the resonator itself with the coupling mediated via virtual transitions. In such a scenario, a different approach is needed to compute interqubit coupling mediated by a ring resonator.

A more accurate way to analyze the ring-resonator-based coupler is to consider wave interference between two independent paths connecting any pair of qubits [26,27]. We start by considering only two transmon [28] qubits in a ring of circumference L and calculate the exchange coupling using a linearized model [29,30]. We place the two qubits at an arbitrary angle θ with respect to each other so that they are connected by two transmission lines of characteristic impedance Z_R and lengths $\ell = (\theta/2\pi)L$ and $\ell' = [1-(\theta/2\pi)]L$ as shown in Fig. 2(a). We denote the modes of the ring resonator by $\{\omega_R^0, \omega_R^1, \ldots, \omega_R^n, \ldots\}$ and the qubit frequencies are chosen between the first two modes of the ring resonator.

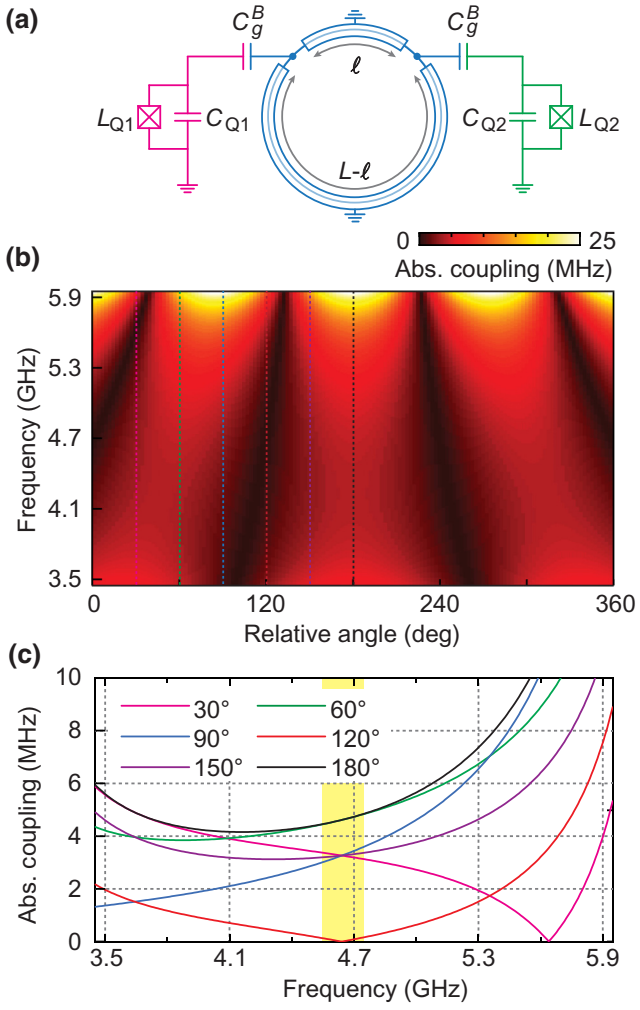

FIG. 2. (a) Circuit schematic showing a pair of qubits (magenta and green) connected to the ring resonator (blue) with the fundamental mode at 3.1 GHz. Interqubit angle $\theta = 2\pi\ell/L$ determines the coupling between the pair of qubits at a particular frequency. (b) Numerical estimation of interqubit coupling as a function of qubit frequency and the angular separation between two identical qubits. The qubits are operated near the mean of the two modes of the bus resonator. (c) Vertical line cuts of plot *B* for six specific angles spaced 30° apart along the ring, showing interqubit coupling as a function of qubit frequency. Ideal range of operating frequencies for qubits with minimal coupling variation is highlighted in yellow.

We compute the interqubit coupling J_{ij} (see Appendix A for details) and plot it as a function of interqubit angle and qubit frequencies ω_Q in Fig. 2(b). We observe that the interqubit coupling varies significantly with frequency and relative qubit position. However, within a certain range of frequencies away from the resonant modes of the ring, the interqubit coupling is reasonably flat except near angles 120° and 240°. If we choose 30° angular spacing between qubits and operate around frequency $\tilde{\omega}_Q = \left(\omega_R^0 + \omega_R^1\right)/2$, connected pairs have only two different values of finite coupling. The vertical line cuts in Fig. 2(b) are separately plotted in Fig. 2(c) to highlight the coupling as a function of qubit frequencies for these angles. Qubit pairs placed at 60°, 180°, and 300° show a maximum value of coupling while those placed at 30°, 90°, 150°, 210°, 270°, and 330° show a coupling reduced by a factor of $\sqrt{2}$ compared to the maximum value. However, the qubits placed at 120° and 240° show zero coupling at this special frequency $\tilde{\omega}_Q$ due to destructive interference of the two paths connecting the two qubits [26]. Thus in a qubit network realized with this particular geometry, each of the 12 qubits is coupled to nine other qubits [Fig. 1(c)]. Further, the interqubit coupling is a slowly varying function of qubit frequency around $\tilde{\omega}_Q$ and thus allows us enough flexibility in the choice of qubit frequencies with a nominal variation in the interqubit coupling [less than ±10% in a range of ±100 MHz; the region highlighted in yellow in Fig. 2(c)].

III. EXPERIMENTAL DEMONSTRATION OF INTERQUBIT COUPLING

In our experiment, we use the 3D circuit QED architecture [31,32] consisting of a central circular bus resonator realized in rectangular coax geometry with 12 slots distributed along its perimeter at 30° angular spacing where the qubit chips can be placed. Twelve $\lambda/4$ resonators adjacent to each slot provides the ability for independent measurement of each qubit [33]. The symmetry of the design ensures that only four qubits are sufficient to explore all six possible combinations of interqubit angles in this design. These four qubits are placed at positions 1, 3, 9, and 10, as shown in Fig. 3(a) and we label them as Q1, Q3, Q9, and Q10, respectively. The remaining qubit positions are filled with dummy silicon chips to retain the symmetry of the ring-resonator modes. Details of the design and assembly are discussed in Appendix C. The fundamental mode

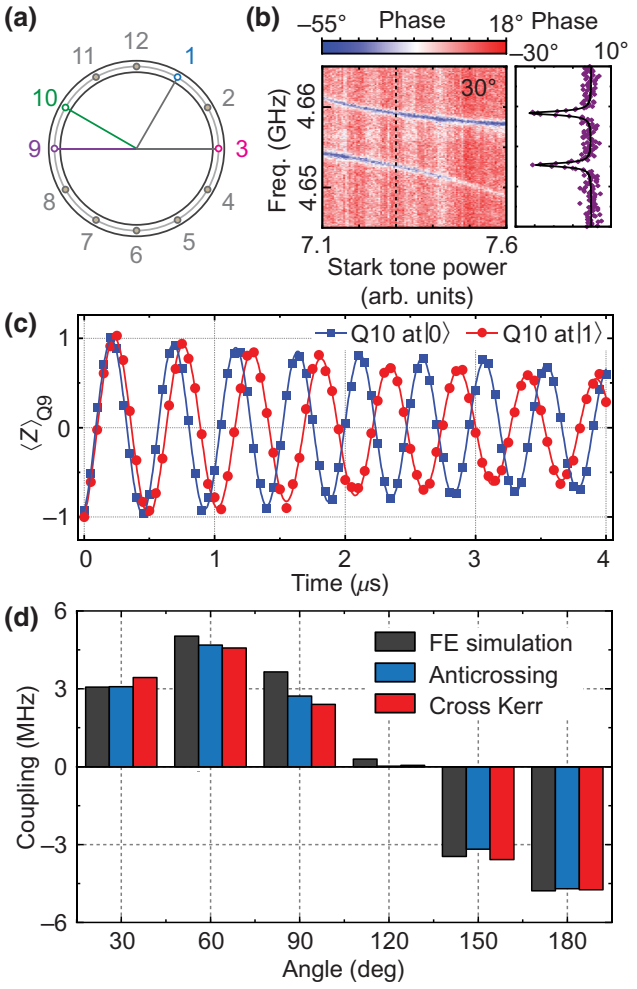

FIG. 3. Measurement of interqubit coupling. (a) The relative locations of the four qubits coupled with the ring resonator that allow measuring all six possible combinations in the current setup. (b) An anticrossing between the pair Q9 and Q10 observed while Stark shifting the transmon Q10 and performing a spectroscopy on Q9. A vertical line cut showing the hybridized states of two qubits in the right panel when they are brought on resonance. (c) A set of conditional Ramsey fringes obtained for the pair Q9 and Q10 in the conditional Ramsey experiment. The measured cross-Kerr shift is used to estimate the interqubit coupling.(d) Interqubit couplings between all possible pairs estimated from the finite-element simulation of the structure and experimentally measured using anticrossing and by conditional Ramsey experiment.

and the first harmonic of the bus resonator are measured at 3.127 and 6.240 GHz in a separate experiment. All device parameters and coherence properties extracted from the experiments are listed in Table I in Appendix C.

We measure the vacuum Rabi splitting between a pair of qubits by tuning them into resonance. All qubits are tuned by applying an off-resonant ac Stark shift tone detuned by $\Delta_S/2\pi \simeq 250$ MHz from the qubit's original transition frequency. We perform spectroscopy on one of the qubits while varying the amplitude of the Stark shift tone to obtain the vacuum Rabi-splitting spectrum of the hybridized qubits [see Fig. 3(b)]. The minimum vacuum Rabi splitting on each pair is measured while parking the spectator qubits at particular frequencies away from the crossing point. Finally, we estimate the transverse coupling strengths J_{ij}, that provide the best match with the experimentally observed splittings by numerically solving the following Hamiltonian for the four-qubit system

$$\hat{\mathcal{H}}_0/\hbar = \sum_{i=1}^{4}[\omega_i \hat{a}_i^\dagger \hat{a}_i + \frac{\delta_i}{2}\hat{a}_i^\dagger \hat{a}_i(\hat{a}_i^\dagger \hat{a}_i - \mathbf{I})] + \sum_{i<j,j=1}^{4} J_{ij}(\hat{a}_i^\dagger \hat{a}_j + \hat{a}_j^\dagger \hat{a}_i). \quad (1)$$

Here ω_i and δ_i are the transition frequency and anharmonicity of the ith transmon, respectively, and J_{ij} is the pairwise exchange coupling between ith and j th transmon. See Appendix E for more details.

We perform another experiment, which uses the cross-Kerr effect between pairs of qubits, to estimate J_{ij} and obtain similar results. The pairwise cross-Kerr shift is measured by using a conditional Ramsey sequence on one qubit while keeping the other qubit in $|0\rangle$ and $|1\rangle$, respectively, as shown in Fig. 3(c). The extracted values of J_{ij} obtained for each pair from the two experiments along with the results from finite-element simulation are plotted in Fig. 3(d) (the raw data for all pairs are shown in the Supplemental Material [34]). The values exhibit good agreement with the theoretical model for the given frequency range, confirming the highest coupling strengths for pairs at 60° and 180°, intermediate coupling strengths for 30°, 90°, and 150° and a negligible coupling for the pair at 120°. We observe small deviations in coupling when compared to finite-element simulations, which is due to variability in the qubit chip dimensions and misalignment of qubit chips while positioning them in the slots. Further, the couplings extracted from finite-element simulations are slightly different from ideal theoretical predictions due to the asymmetry introduced by the three sapphire chips used to mount the central ring. In addition the cross-Kerr effect is sensitive to the ring-resonator response at qubit transition frequencies from $|1\rangle$ to $|2\rangle$ as well and that effect is not included in our theory (see Appendix D for details).

We also characterize the microwave crosstalk between the qubits at readout frequencies as well as at qubit frequencies and observe a negligible classical crosstalk in our setup. This can be attributed to two different features of our system. Firstly, the 3D cQED setup offers better microwave isolation for individual qubits with more precise control of the microwave environment. In addition, the qubits are spaced further apart from each other due to uniform distribution along the ring. This suppresses the direct

radiative coupling between the qubits leading to further reduction of microwave crosstalk. The spatial separation will help achieve low microwave crosstalk even in the 2D geometry. Details of the crosstalk measurements are given in Appendices F and G.

IV. SCALING UP TO LARGER QUBIT NETWORKS

The unique ability to couple several non-nearest-neighbor qubits demonstrated in this architecture readily suggests multiple potential extensions to achieve highly connected quantum processors. Simply putting more qubits in the existing design (with reduced angular spacing) will introduce a wider variation of coupling. Instead, we propose two extensions, which also provide only two values of interqubit coupling between different pairs. Further, we suggest using a tunable coupler between each qubit and the ring resonator to turn on couplings only between the intended qubits while keeping the other qubits completely isolated. This will provide maximum flexibility for different applications.

The simplest extension is to increase the length of the ring resonator, e.g., using one with the fundamental mode $\omega_R^0 = 1$ GHz, which can contain 36 qubits with 10° angular spacing. The qubits are now operated between the third and fourth harmonics of the ring resonator around the mean frequency $\tilde{\omega}_Q = (\omega_R^3 + \omega_R^4)/2 = 4.5$ GHz. In this geometry every qubit is connected to 27 other qubits in the network with only two different values of coupling as shown by the solid and dotted connections in Fig. 4(a). The dependence of the coupling on frequency around the special point is numerically calculated and plotted in Fig. 4(b). However, as shown in the figure, the frequency dependence of the coupling around the special operating point grows stronger as the fundamental frequency of the ring resonator

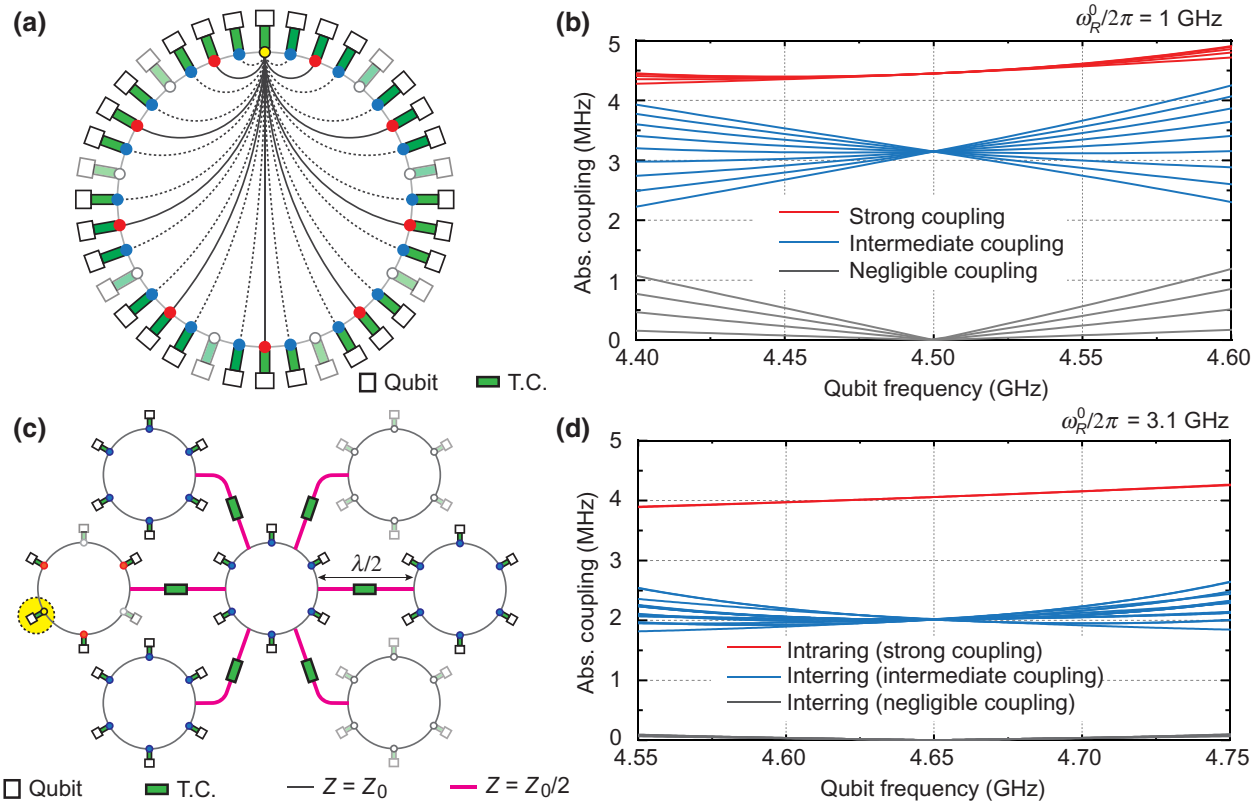

FIG. 4. Scaling to a larger number of qubits. (a) A larger ring with the fundamental mode at $\omega_R^0/2\pi = 1$ GHz, accommodating 36 qubits. The qubit frequencies are chosen around the special frequency at the mean of two higher harmonics ω_R^3 and ω_R^4 of the ring resonator. A tunable coupler is suggested to control the coupling of each qubit to the network. (b) Variation of interqubit coupling around the special point for the larger ring architecture. Each qubit is connected to 27 other qubits in the ring with only two different values of couplings shown in red and blue at the special frequency. (c) A multiring architecture with 42 qubits placed at the marked positions. Each of the rings has a fundamental mode at $\omega_R^0/2\pi = 3.1$ GHz with the operating frequency at 4.65 GHz. Two rings are connected via a $\lambda/2$ section of transmission line with a characteristic impedance equal to half that of the ring resonators. Additional tunable couplers can be integrated with the $\lambda/2$ sections to isolate parts of the network on demand for parallel multiqubit operations. (d) Variation of coupling for different set of qubit pairs marked in (c). All the qubits placed in the position marked with blue share identical coupling at the special frequency whereas the positions marked with red share a higher coupling. The faded out qubits are not coupled to the highlighted qubit.

is pushed down to accommodate a larger number of qubits. Consequently one cannot push this method to a very large number of qubits. Further, since all the qubits share the same ring, it will be challenging to implement parallel two-qubit gates among independent pairs of qubits. However, this extension may be useful for quantum simulations and quantum many-body physics experiments, which require many-body interactions [14].

The second extension uses multiple identical ring resonators containing six qubits each and connected to each other by $\lambda/2$ sections where λ is wavelength of the fundamental mode of the ring resonator [See Fig. 4(c)]. The connecting $\lambda/2$ section has a characteristic impedance half that of the ring resonators. In this design with 42 qubits, each qubit in the outer ring is connected to 27 other qubits whereas each qubit in the central ring is connected to 39 other qubits. We numerically calculate the frequency dependence of the coupling for different qubit locations and plot them in Fig. 4(d), showing two different coupling values for interring and intraring qubits, respectively. The detailed calculations related to these two extensions are discussed in Appendix B. As shown, one can also integrate tunable couplers in the $\lambda/2$ sections to isolate different parts of the multiqubit network [35] for parallel operations. Since the interqubit coupling strength will keep falling for qubits in distant rings, this method cannot provide arbitrarily long-range coupling. However, unlike existing architectures, it can provide dense connectivity locally in a larger multiqubit network.

V. CONCLUSION

In summary, we introduce a powerful coupling architecture using a ring resonator to realize a highly connected qubit network for superconducting circuits. We analyze the interqubit coupling by considering two interfering paths connecting a pair of qubits. Our 3D cQED implementation of a system capable of supporting 12 qubits confirms the theoretical prediction that each qubit will be connected to nine other qubits with only two values of finite coupling strength. This is achieved by a careful choice of operating frequency and qubit position on the ring. We also calculate the interqubit coupling for larger qubit networks involving larger-sized rings and multiple rings connected to each other, suggesting scalability of this idea. The unique feature offered by this design can be easily translated to a wide range of qubits [28,36,37], implemented in both 2D [25] and 3D layout and adapted to any platform, which relies on a resonator bus for mediating interqubit coupling. This will substantially enhance the performance of present-day quantum processors without any added topological complexity or control wiring overhead. We anticipate that the enhanced qubit connectivity will have a significant impact in the field of quantum simulations [38] and error correction [39].

ACKNOWLEDGMENTS

We acknowledge the nanofabrication and central workshop facilities of TIFR. We thank Mandar Deshmukh, Michel Devoret, and Kater Murch for useful inputs on the paper. This work is supported by the Department of Atomic Energy of the Government of India under Project No. RTI4003. We also acknowledge support from the Department of Science and Technology, India, via the QuEST program.

Note added:— Recently we became aware of similar work [25] where the authors couple two qubits with a ring resonator in 2D geometry.

APPENDIX A: EVEN- AND ODD-MODE ANALYSIS OF THE RING RESONATOR

In order to theoretically investigate the coupling between any arbitrary pair of qubits connected to the ring at some particular angle, we first extract the *ABCD* matrix of the network between any two points of the ring resonator, shown in the dashed box in Fig. 5(a). We use this symmetry of the system to decompose it into a superposition of two simpler circuits, as shown in Fig. 5(b). We define two different modes of excitation for the circuit [40]; the even mode where $V_{g1} = V_{g2} = V/2$, and the odd mode, where $V_{g1} = -V_{g2} = V/2$. Now, from the superposition of these two modes we get an excitation $V_{g1} = V$ and $V_{g2} = 0$. We define the impedance of the ring resonator as Z and now treat the two modes separately.

For the even mode of excitation, $V_{g1} = V_{g2} = V/2$, so there is no current flowing through the arms of the resonator. Therefore, we can bisect the ring along the vertical symmetry axis with open circuits at the points of bisection. Similarly, for the odd mode of excitation, $V_{g1} = -V_{g2} = V/2$, and hence there is a voltage null at the points of bisection. Therefore, we can ground the central pin at these two points of the resonator, leading to short circuit.

As shown in Fig. 5(a), the two qubits are connected to each other by two sections of transmission line of length $\ell = L(\theta/\pi)$ and $L - l$, where L is the total circumference of the ring and θ is the angular separation between the two qubits in radians. We use the impedance transformation formula to get the effective impedance of the short and open circuit at the end of a transmission line of characteristic impedance Z_R and length x.

$$Z_{\text{in}} = Z_R \frac{Z_L + jZ_R \tan \beta x}{Z_R + jZ_L \tan \beta x}, \tag{A1}$$

where, $\beta = 2\pi/\lambda$ and the load impedance, Z_L is equal to 0 and ∞, respectively, for the short circuit (odd) and the open circuit (even) case. This leads to $Z_{\text{in}}^{\text{open}} = -jZ_R \cot \beta x$ and $Z_{\text{in}}^{\text{short}} = jZ_R \tan \beta x$. For the even and odd mode the effective impedance is the parallel combination of two transmission lines of lengths $x_1 = \ell/2$ and

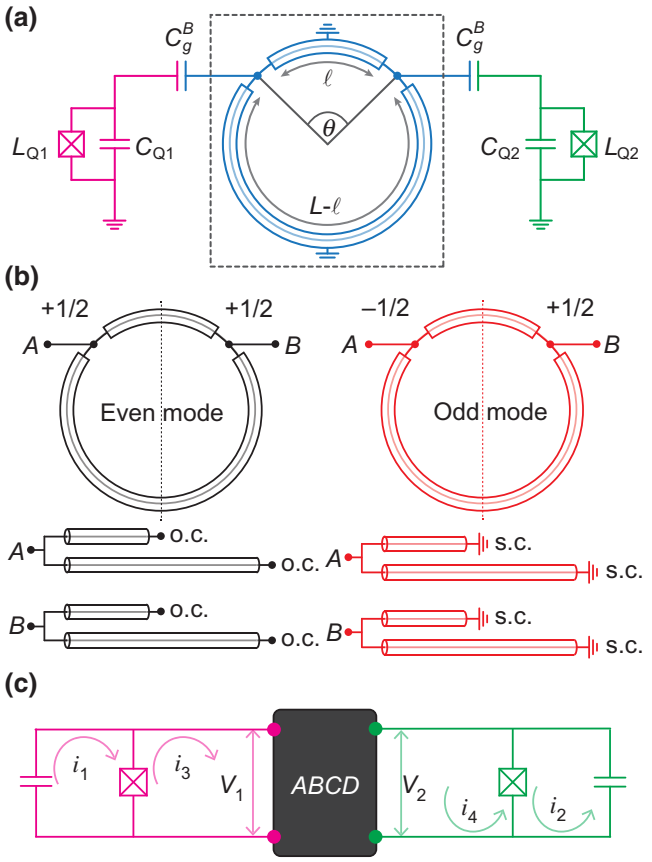

FIG. 5. (a) Circuit schematic showing a pair of qubits (magenta and green) connected to the ring resonator (blue). Qubits are operated around the mean frequency of the first two modes of the ring resonator. (b) Breaking down the ring resonator into a superposition of two simpler circuits named even and odd modes. (c) Solving the coupled qubit system using the ring resonator as the coupling element. The ring is treated as a two-port black box with given network parameters. The junctions are treated as linear inductors.

$x_2 = (L - \ell)/2.$

$$Z^e_{\rm tot} = -jZ_R \frac{\cot(\beta\ell/2) \times \cot[\beta(L-\ell)/2]}{\cot(\beta\ell/2) + \cot[\beta(L-\ell)/2]},$$
$$Z^o_{\rm tot} = jZ_R \frac{\tan(\beta\ell/2) \times \tan[\beta(L-\ell)/2]}{\tan(\beta\ell/2) + \tan[\beta(L-\ell)/2]}. \tag{A2}$$

Defining $a(\omega) = \tan(\beta\ell/2)$ and $b(\omega) = \tan[\beta(L-\ell)/2]$ and substituting in Eq. (A2), we derive the expressions for the reflections at the port for even and odd mode,

$$\Gamma^e(\omega) = \frac{-jZ_R/[a(\omega)+b(\omega)] - Z_0}{-jZ_R/[a(\omega)+b(\omega)] + Z_0} = \frac{jr + [a(\omega)+b(\omega)]}{jr - [a(\omega)+b(\omega)]} \tag{A3}$$

$$\Gamma^\circ(\omega) = \frac{jZ_R/\left[a(\omega)^{-1}+b(\omega)^{-1}\right] - Z_0}{jZ_R/\left[a(\omega)^{-1}+b(\omega)^{-1}\right] + Z_0} = \frac{jra(\omega)b(\omega) - [a(\omega)+b(\omega)]}{jra(\omega)b(\omega) + [a(\omega)+b(\omega)]},$$

where Z_0 is the port impedance and $r = Z_R/Z_0$. The complex amplitude of the scattered waves at port 1 and port 2 are given by the symmetric and antisymmetric superposition of the reflection coefficients $\Gamma^e(\omega)$ and $\Gamma^\circ(\omega)$ for the even and odd modes, respectively,

$$K_1 = \frac{1}{2}\Gamma^e(\omega) + \frac{1}{2}\Gamma^\circ(\omega),$$
$$K_2 = \frac{1}{2}\Gamma^e(\omega) - \frac{1}{2}\Gamma^\circ(\omega). \tag{A4}$$

The *ABCD* matrix between the two ports attached to the ring resonator is then written as [40]

$$ABCD_{\rm ring} = \begin{pmatrix} A_r & B_r \\ C_r & D_r \end{pmatrix} = \frac{1}{2K_2}\begin{pmatrix} \left(1 - K_1^2 + K_2^2\right) & Z_0\left(1 + K_1^2 - K_2^2\right) \\ \left(1 - K_1^2 - K_2^2\right)/Z_0 & \left(1 - K_1^2 + K_2^2\right) \end{pmatrix}. \tag{A5}$$

Note that at the special frequency $\omega_{\rm sp} = 3\omega_0/2$, where ω_0 is the fundamental mode of the ring resonator, the *ABCD* matrix of the ring is reduced to a simple form:

$$ABCD_{\rm sp} = \begin{pmatrix} 0 & jZ'(\theta) \\ jY'(\theta) & 0 \end{pmatrix}, \tag{A6}$$

where, $Z'(\theta) = 1/Y'(\theta) = [(Z_R/2)\sin(3\theta/2)]$ and θ is the angular spacing between the qubits in radians.

It is also evident from Eq. (A6) that choosing θ at the interval of $\pi/6$ limits the variation of the parameter Z' to a few values: $Z'(2\pi/3) = 0$, $Z'(\pi/3) = -Z'(\pi) = Z'_{\rm max}$ and $Z'(\pi/6) = Z'(\pi/2) = -Z'(5\pi/6) = (Z'_{\rm max}/\sqrt{2})$, where $Z'_{\rm max} = Z_R/2$. This leads to the fact that the magnitude of the coupling between connected pairs shows only two different values at the special frequency as mentioned in the main text.

However, in addition to computing the coupling at the special frequency, we are also interested in finding the variation of coupling as we move away from this point. Hence, we continue using the general expression for the *ABCD* matrix of the ring as given by Eq. (A5) in the rest of the analysis. The qubits are introduced in the circuit and are approximated as linear resonators by replacing the Josephson junction with a linear inductor. The qubits are capacitively coupled to the ring resonator with a coupling capacitance C_g^B. The *ABCD* matrix of the coupling capacitance is written as

$$ABCD_{C_g^B} = \begin{pmatrix} 1 & -j/(\omega C_g^B) \\ 0 & 1 \end{pmatrix} \tag{A7}$$

and can be absorbed into a combined *ABCD* matrix containing the ring resonator and the two coupling capacitors. The combined *ABCD* matrix is defined as

$$\begin{aligned} ABCD_{\text{comb}} &= \begin{pmatrix} \tilde{A} & \tilde{B} \\ \tilde{C} & \tilde{D} \end{pmatrix} \\ &= \begin{pmatrix} 1 & -j/(\omega C_g^B) \\ 0 & 1 \end{pmatrix} \begin{pmatrix} A_r & B_r \\ C_r & D_r \end{pmatrix} \begin{pmatrix} 1 & -j/(\omega C_g^B) \\ 0 & 1 \end{pmatrix}. \end{aligned} \tag{A8}$$

Substituting for the values of A_r, B_r, C_r, and D_r from Eq. (A5) and simplifying, we get,

$$\begin{aligned} \tilde{A} &= \frac{2\,[a(\omega)+b(\omega)] + C_g^B Z_R \omega\,[1-a(\omega)b(\omega)]}{C_g^B Z_R \omega\,[1+a(\omega)b(\omega)]} \\ \tilde{B} &= j\,\frac{2C_g^{B2} Z_R^2 \omega^2 a(\omega)b(\omega) - 2\,[a(\omega)+b(\omega)]^2 + 2Z_R \omega C_g^B\,[a(\omega)+b(\omega)]\,[a(\omega)b(\omega)-1]}{C_g^{B2} Z_R \omega^2\,[a(\omega)+b(\omega)]\,[1+a(\omega)b(\omega)]} \\ \tilde{C} &= \frac{2j}{Z_R} \times \frac{a(\omega)+b(\omega)}{1+a(\omega)b(\omega)} \\ \tilde{D} &= \frac{2\,[a(\omega)+b(\omega)] + C_g^B Z_R \omega\,[1-a(\omega)b(\omega)]}{C_g^B Z_R \omega\,[1+a(\omega)b(\omega)]}. \end{aligned} \tag{A9}$$

We then write down the coupled equations of the complete circuit consisting of the pair of linearized qubits and the ring resonator in the frequency domain. The coupling between the pair of qubits is mediated by the *ABCD* matrix given by Eq. (A9) for the two-port network shown in Fig. 5(c). The inductance and capacitance of the qubits are given by $L_Q = \phi_0^2/E_J$ and $C_Q = e^2/2E_C$, respectively, where E_J is the Josephson energy, E_C is the electrostatic charging energy of the oscillators, and $\phi_0 = \hbar/2e$ is the reduced flux quantum.

$$\begin{aligned} \frac{i_1}{j\,\omega C_{Q1}} + j\,\omega L_{Q1}\,(i_1 - i_3) &= 0, \\ \frac{i_2}{j\,\omega C_{Q2}} + j\,\omega L_{Q2}\,(i_2 - i_4) &= 0, \end{aligned} \tag{A10}$$

where i_3 and i_4 are connected by the elements of the *ABCD* matrix of the black box.

$$\begin{pmatrix} i_3 \\ i_4 \end{pmatrix} = \frac{1}{\tilde{B}} \begin{pmatrix} \tilde{D} & \tilde{B}\tilde{C} - \tilde{A}\tilde{D} \\ -1 & \tilde{A} \end{pmatrix} \begin{pmatrix} -i_1/(j\,\omega C_{Q1}) \\ -i_2/(j\,\omega C_{Q2}) \end{pmatrix}. \tag{A11}$$

The coupled Eqs. (A10) are now written as

$$\begin{aligned} &\frac{i_1}{C_{Q1}}\tilde{B} + j\,\omega \frac{L_1}{C_{Q1}} i_1 \tilde{D} - \omega^2 L_1 i_1 \tilde{B} \\ &\quad + j\,\omega \frac{L_1}{C_{Q2}} i_2 (\tilde{B}\tilde{C} - \tilde{A}\tilde{D}) = 0, \\ &\frac{i_2}{C_{Q2}}\tilde{B} + j\,\omega \frac{L_2}{C_{Q2}} i_2 \tilde{A} - \omega^2 L_2 i_2 \tilde{B} - j\,\omega \frac{L_2}{C_{Q1}} i_1 = 0. \end{aligned} \tag{A12}$$

Dividing the equations by L_1 and L_2, respectively, and using qubit frequencies, $\omega_{q,m} = (L_m C_m)^{-1/2}$ we have

$$\begin{aligned} \left(\tilde{B}\omega_{q1}^2 + \frac{j\,\omega}{C_{Q1}}\tilde{D} - \omega^2\tilde{B}\right) i_1 + \frac{j\,\omega}{C_{Q2}}(\tilde{B}\tilde{C} - \tilde{A}\tilde{D}) i_2 &= 0, \\ -\frac{j\,\omega}{C_{Q1}} i_1 + \left(\tilde{B}\omega_{q2}^2 + \frac{j\,\omega}{C_{Q2}}\tilde{A} - \omega^2\tilde{B}\right) i_2 &= 0. \end{aligned} \tag{A13}$$

The eigenmodes $\{\omega_\lambda\}$ of the system are found by solving the determinant $|\mathcal{M}_{2\times 2}| = 0$, where $\mathcal{M}_{2\times 2}$ is given by

$$\begin{aligned}\mathcal{M}_{11} &= \tilde{B}(\omega_{q1}^2 - \omega^2) + \frac{j\omega}{C_{Q1}}\tilde{D},\\ \mathcal{M}_{12} &= \frac{j\omega}{C_{Q2}}\left(\tilde{B}\tilde{C} - \tilde{A}\tilde{D}\right),\\ \mathcal{M}_{21} &= -\frac{j\omega}{C_{Q1}},\\ \mathcal{M}_{22} &= \tilde{B}(\omega_{q2}^2 - \omega^2) + \frac{j\omega}{C_{Q2}}\tilde{A}.\end{aligned} \tag{A14}$$

When the two qubits are set identical, the splitting between the two eigenfrequencies corresponding to the qubit modes is given by $\Delta = 2J_{ij}$, where J_{ij} is the interqubit coupling at the mean of the two frequencies.

APPENDIX B: SCALING UP TO MORE QUBITS

To scale up, one of the proposed schemes in the main text is the use of a larger ring having the fundamental mode at 1 GHz and qubits placed at 10° angular spacing. The special operating point is now at the mean of the third and fourth harmonics, i.e., $\tilde{\omega}_Q = (\omega_R^3 + \omega_R^4)/2 = 4.5$ GHz. We use the same treatment as mentioned above to generate the interqubit coupling as a function of frequency and angle. Any qubit [e.g., one highlighted in yellow, in Fig. 4(a) of the main text] is connected to 27 other qubits in the ring. In this longer ring, qubits spaced by 40° to each other show negligible coupling. The remaining qubits are connected with two slightly different values of coupling at $\tilde{\omega}_Q$, shown as red and blue dots in the figure representing the stronger and weaker coupling, respectively. However, the longer ring resonator results in a reduced window for the choice of qubit frequencies as the coupling values deviate a lot faster as one moves from the special frequency. This is due to a smaller spacing between the successive harmonics of the ring resonator, leading to stronger variation of coupling with frequency.

The other approach involves multiple ring cavities with each pair of rings connected via a $\lambda/2$ resonator resonating at the fundamental mode of the ring resonator. The characteristic impedance of the $\lambda/2$ section is chosen to be $Z_C = Z_R/2$ so that the impedance is matched and there is no reflection at the junction. We first investigate the case of two connected ring resonators using the *ABCD* matrices of individual sections. The combined *ABCD* matrix between the two qubits connected at arbitrary locations of two different rings can be written as

$$\begin{aligned}ABCD_{\text{ext}} = &\begin{pmatrix}1 & -j/(\omega C_g^B)\\ 0 & 1\end{pmatrix}\begin{pmatrix}A_{r1} & B_{r1}\\ C_{r1} & D_{r1}\end{pmatrix}\begin{pmatrix}A_{\lambda/2} & B_{\lambda/2}\\ C_{\lambda/2} & D_{\lambda/2}\end{pmatrix}\\ &\times\begin{pmatrix}A_{r2} & B_{r2}\\ C_{r2} & D_{r2}\end{pmatrix}\begin{pmatrix}1 & -j/(\omega C_g^B)\\ 0 & 1\end{pmatrix},\end{aligned} \tag{B1}$$

where the *ABCD* matrix with subscript $r1(r2)$ corresponds to the two-port network between the qubit and the point where the $\lambda/2$ section is connected to the first (second) ring resonator. The *ABCD* matrix with subscript $\lambda/2$ corresponds to the section between the two ends of the $\lambda/2$ resonator and is given by

$$\begin{pmatrix}A_{\lambda/2} & B_{\lambda/2}\\ C_{\lambda/2} & D_{\lambda/2}\end{pmatrix} = \begin{pmatrix}\cos(\beta L_{\lambda/2}) & jZ_C\sin(\beta L_{\lambda/2})\\ (j/Z_C)\sin(\beta L_{\lambda/2}) & \cos(\beta L_{\lambda/2})\end{pmatrix}, \tag{B2}$$

where $L_{\lambda/2}$ is the length of the $\lambda/2$ section.

The coupled equations of motion for the two qubits are written in terms of $\mathcal{M}$ given by Eq. (A14) where we substitute the expressions for $\tilde{A}$, $\tilde{B}$, $\tilde{C}$, and $\tilde{D}$ from Eq. (B1). Finally, the interqubit coupling is computed by bringing the qubits on resonance and measuring the splitting of the qubit normal modes by solving $|\mathcal{M}_{2\times2}| = 0$.

We can use this approach to analyze the full network shown in Fig. 4(c) of the main text. The central ring resonator is connected to six outer ring resonators by $\lambda/2$ sections. The connections are made to the central ring at 60° angular separations. The remaining positions on the central ring resonator are connected to qubits and six qubits are placed at each of the outer ring resonators uniformly with the first qubit anchored at the 30° angular position from the connecting point. We highlight one qubit in one of the outer rings with yellow in Fig. 4(c) of the main text and show its connectivity to all other qubits in the network. Each qubit is connected to three other qubits sharing the same ring at the locations marked with red dots. Additionally, it is connected to every qubit in the central ring as well as three other outer rings (marked with blue dots). However, all qubits (faded out in the diagram) placed in the two remaining outer rings are completely decoupled from the highlighted qubit. This happens due to the same destructive interference effect discussed earlier, as those two rings are connected to the central ring at 120° angles with respect to the one containing the highlighted qubit. The qubits are operated around the mean frequency $\tilde{\omega}_Q = (\omega_R^0 + \omega_R^1)/2$ of the first two modes of the ring resonators. Remarkably, at the special frequency $\tilde{\omega}_Q$, the interqubit couplings share only two different values as before, a higher value for qubits within the same ring and a lower value for qubits from different rings, distinguished by the red and blue dots in the figure.

APPENDIX C: DEVICE DESIGN AND PARAMETERS

Our experimental design consists of a central circular bus resonator with 12 slots distributed along its perimeter to place the qubits with an angular spacing of 30°. Each qubit slot is attached to a dedicated $\lambda/4$ readout resonator extending radially outward as shown in Fig. 6(b). Both the bus resonator and the readout resonators are realized in rectangular coaxial transmission line geometry.

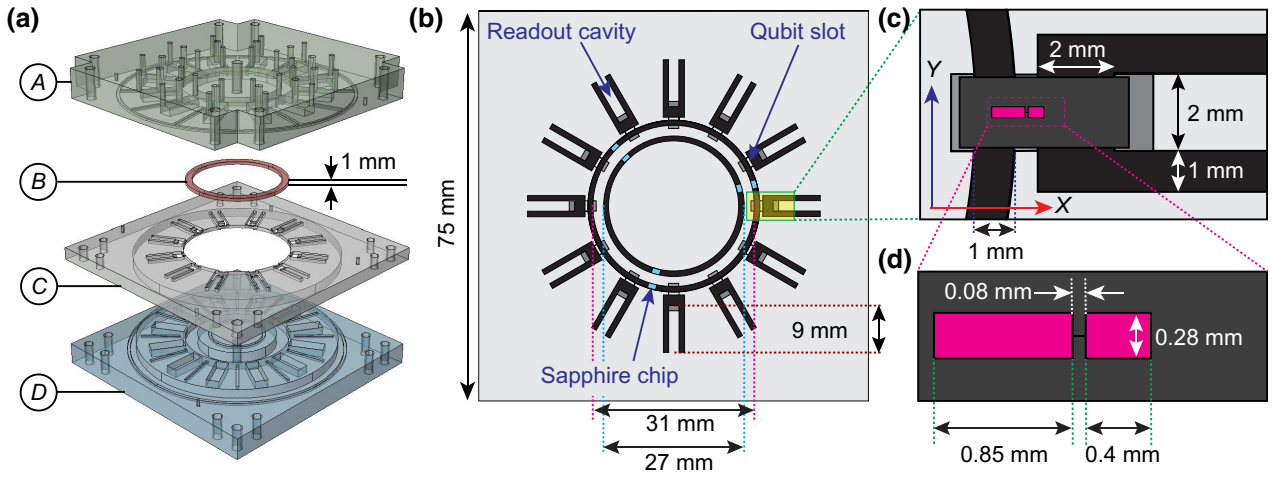

FIG. 6. Design and assembly of the 3D ring resonator setup. (a) The device is machined in four parts labeled (A)–(D). Parts (A) and (D) contain the top and bottom parts, respectively, of the ring resonator and the readout cavities. Part (B) is the central conductor of the ring resonator. Part (C) contains the central conductor of the readout cavities and the slots for placing the qubits. The SMA connectors (not shown) for the readout cavities are attached to part (A) from the top and bring in the readout and qubit excitation. (b) Top view of the ring-resonator setup after assembling parts (B)–(D). The dimensions of the bus and readout cavities are shown. Three sapphire chips (shown in cyan) hold the central conductor of the bus resonator in position. (c) Magnified view of a qubit chip placed in its slot shared between the bus and readout cavities. (d) Magnified view of the transmon qubit design showing the capacitor pad dimensions used in the experiment.

Coupling ports for readout and qubit drive are introduced along the third dimension, offering in-plane scalability and convenient 3D integration for control lines.

The ring resonator is designed in four parts and individual parts are machined from aluminum. As shown in Fig. 6(a), the top- and bottom-most pieces contain the top and bottom halves of the ring and readout cavities. The ring-shaped central conductor is placed in the bottom piece and rests on three sapphire holder chips as indicated in the figure. The sapphire chips are glued to the bottom piece and the ring is glued to the sapphire chips using a small amount of Stycast 2850FT. It is carefully placed in position under an optical microscope so that it rests symmetrically. The central piece contains the central conductors of all the 12 readout cavities. They are designed to have nominally identical lengths and hence identical resonant frequencies. The actual machined piece has some unavoidable variations in the dimensions due to machining tolerances. The dimensions of the ring and the readout cavities are indicated in Fig. 6(b). Once the ring is in place, the central piece is bolted to the bottom piece with four screws. The qubit chips can now be placed in the respective slots as indicated in Fig. 6(c). This operation is also carried out using an optical microscope for precise placement of the chips and we use *N* grease to keep the chips in place. After the qubit chips are placed, the top piece is bolted to the rest of the assembly with nine screws. As can be seen in Fig. 6(a), several grooves are provided for indium sealing

TABLE I. Measured device parameters and coherence times of the four transmons used in the experiment. The qubit-readout cavity coupling is estimated by measuring the shift in the cavity frequency when probed at low power and high power. Ramsey fringes of the qubits marked with asterisk show beating leading to deterioration of Ramsey time which improves significantly with an echo sequence.

Measured parameters	Qubit 1 (Q1)	Qubit 3 (Q3)	Qubit 9 (Q9)	Qubit 10 (Q10)
Qubit frequency, $\omega_q/2\pi$ (GHz)	4.6376	4.5932	4.6566	4.7488
Anharmonicity, $\delta_q/2\pi$ (GHz)	−0.318	−0.306	−0.309	−0.308
Readout resonator frequency, $\omega_R/2\pi$ (GHz)	7.5500	7.5650	7.4744	7.5095
Readout resonator linewidth, $\kappa_R/2\pi$ (MHz)	3.27	4.01	4.78	2.04
Qubit-readout coupling, $g/2\pi$ (MHz)	71	55	73	79
Relaxation time, T_1 (μs)	41	31	37	35
Ramsey time, T_2^R (μs)	3.4	2.6*	6.0*	3.6*
Hahn echo time, T_2^E (μs)	8	24	20	29

to create appropriate microwave isolation for all readout cavities and the central ring resonator as well.

The measured device parameters and coherence numbers are listed in Table I.

APPENDIX D: TUNING QUBIT-CAVITY COUPLINGS

The capacitor pads of the qubits are designed based on finite-element simulation of the complete qubit-cavity system to yield desired qubit-readout coupling and interqubit coupling. The qubit junction sits on the bridge [33] between the readout cavity and the bus resonator and the dimension of the capacitor pad extending into respective cavities determines the magnitudes of the couplings. In the finite-element simulation we eliminate the Josephson junction and introduce a port across the junction terminals and extract the full scattering matrix of the system. To estimate the qubit-readout cavity coupling we terminate the readout cavity port with a 50 Ω load and compute the resulting Purcell T_1 decay time as a function of the detuning between the qubit and the readout cavity. We then fit this to the Purcell T_1 formula to extract the coupling.

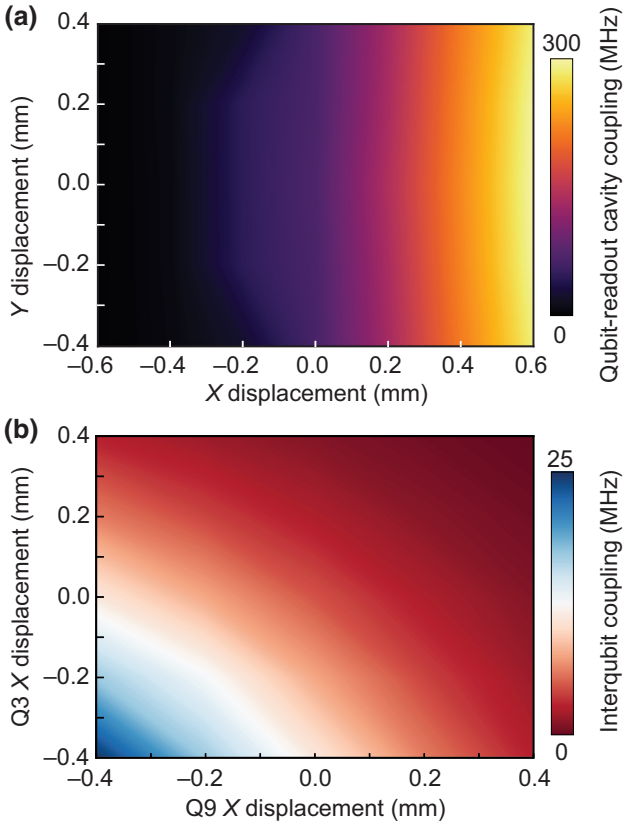

FIG. 7. Tolerance in qubit placement estimated from finite-element simulation. (a) Variation of qubit-readout coupling as a function of qubit displacement in the X direction (into and out of the readout cavity) and Y direction (lateral displacement). We find that the coupling is weakly dependent on lateral displacement but it is more sensitive to the in and out displacement of the qubit. (b) Interqubit coupling between the pair Q3–Q9 placed at 180° as a function of X displacement of both the qubits. The displacement determines the coupling with the bus resonator and hence the interqubit coupling. The coupling is sensitive to qubit placement requiring precise placement of the qubits in their respective slots.

We use an avoided crossing simulation to numerically extract the interqubit coupling. We approximate the qubits as harmonic oscillators and introduce two linear inductors to the two-port circuit represented by the scattering matrix. Finally, we bring the two oscillators on resonance by tuning the inductor values to produce an avoided crossing. The interqubit coupling is then estimated from the normal mode splitting.

We also analyze the tolerance of the coupling of qubit to readout cavity and the interqubit coupling to small deviations in placement of the qubits in their slots. In Fig. 7(a) we plot the dependence of the qubit-readout coupling as a function of X and Y displacement [see Fig. 6(c)]. X displacement refers to the direction parallel to the central conductor of the readout resonator; Y displacement is in the direction orthogonal to X. We observe that the coupling is relatively insensitive to Y displacement but it depends strongly on the displacement in X direction. Next we study the dependence of the interqubit coupling on the X displacement of the qubits and the results are shown in Fig. 7(b). The data indicates that chips have to be placed precisely to prevent large deviations in interqubit couplings. We use an optical microscope to place the qubits precisely in their slots.

APPENDIX E: ESTIMATION OF THE INTERQUBIT COUPLING

The effective Hamiltonian of the coupled four transmon system is written as

$$\hat{\mathcal{H}}_0/\hbar = \sum_{i=1}^{N}\left[\omega_i \hat{a}_i^\dagger \hat{a}_i + \frac{\delta_i}{2}\hat{a}_i^\dagger \hat{a}_i(\hat{a}_i^\dagger \hat{a}_i - \mathbf{I})\right] + \sum_{i<j,j=1}^{N} J_{ij}(\hat{a}_i^\dagger \hat{a}_j + \hat{a}_j^\dagger \hat{a}_i), \tag{E1}$$

where a_i and $a_i^\dagger$ are the annihilation and creation operators of the kth transmon, which is modeled as Duffing oscillator, $\tilde{\omega}_i$ and δ_i are the lowest transition frequency and the anharmonicity of the respective ladders. J_{ij} is the exchange coupling between the ith and jth transmons. We neglect the frequency dependence of the exchange coupling in this calculation.

The interqubit coupling terms hybridize the levels and the eigenmodes of the coupled four-transmon system are

TABLE II. Cross-Kerr shift between all qubit pairs measured in the conditional Ramsey experiment and the estimated interqubit coupling J_{ij}.

Qubit pair	Q9-Q10	Q1-Q3	Q1-Q10	Q1-Q9	Q3-Q10	Q3-Q9
Relative angular positions	30°	60°	90°	120°	150°	180°
Measured cross-Kerr shift (kHz)	−102	−140	−28	−5	−104	−146
Estimated interqubit coupling (MHz)	3.45	4.57	2.40	0.05	−3.58	−4.74

obtained by diagonalizing the Hamiltonian in Eq. (E1). In the experiment we extract the effective low-energy levels of the full Hamiltonian in the diagonal (dressed) basis. The problem then reduces to numerically finding the best set of coupling parameters J_{ij} in Eq. (E1) with the measured values of $\tilde{\omega}_i$ and δ_i that would produce the experimentally observed low-energy eigenspectra.

The cross-Kerr shift is a manifestation of the interaction among the doubly excited levels, e.g., $|0002\rangle$, $|0020\rangle$, $|0011\rangle$, $|1001\rangle$ etc. that depends on the exchange coupling J_{ij} and can be measured by a set of conditional Ramsey sequences. The vacuum Rabi splitting experiment is an alternate method to extract the exchange coupling values. The splitting depends on the interaction between the single excitation levels of all the qubits.

While numerically finding the actual interqubit coupling using Eq. (E1), we use 8 levels for each transmon and truncate the total number of excitations in the system at 8. We have also restricted the search space by assigning appropriate polarity of the coupling which is negative for angles between 120° and 240° and positive otherwise. The estimated coupling from the conditional Ramsey experiment between all pairs are listed in Table II.

APPENDIX F: QUBIT DRIVE CROSSTALK

Classical crosstalk due to microwave leakage at qubit frequencies to untargeted qubits may lead to unwanted evolution of the system. We use cross-resonance (CR) [41] interaction in our multiqubit architecture to characterize the classical crosstalk. The CR Hamiltonian is given by

$$H_{\mathrm{CR}}/\hbar = \sum_{k=1,2}\left(\tilde{\omega}_k b_k^\dagger b_k + \frac{\delta_k}{2} b_k^\dagger b_k \left(b_k^\dagger b_k - \mathbf{I}\right)\right) + J\left(b_1^\dagger b_2 + b_2^\dagger b_1\right) + H_d, \tag{F1}$$

where b_k and $b_k^\dagger$ are the annihilation and creation operator of the kth transmon, $\tilde{\omega}_k$ and δ_k are the lowest transition frequency and the anharmonicity of the respective ladders. J is the exchange coupling strength between the two transmons and the drive term H_d is given by

$$H_d = \Omega\cos\left(\tilde{\omega}_2 t + \varphi_0\right)\left(b_1^\dagger + b_1\right) + m\Omega\cos\left(\tilde{\omega}_2 t + \varphi_{\mathrm{CT}}\right)\left(b_2^\dagger + b_2\right), \tag{F2}$$

where the second term is due to microwave crosstalk directly driving the second qubit. The resulting ZX and IX interaction terms can be extracted by an effective Hamiltonian theory and when the drive phase φ_0 is set to zero, the amplitudes of the two terms are given by [42]

$$A_{ZX} = -\frac{J\Omega}{\Delta}\left(\frac{\delta_1}{\delta_1+\Delta}\right) + \frac{J\Omega^3\delta_1^2\left(3\delta_1^3+11\delta_1^2\Delta+15\delta_1\Delta^2+9\Delta^3\right)}{4\Delta^3\left(\delta_1+\Delta\right)^3\left(\delta_1+2\Delta\right)\left(3\delta_1+2\Delta\right)}, \tag{F3}$$

$$A_{IX} = -\frac{J\Omega}{\delta_1+\Delta} + \frac{J\Omega^3\delta_1\Delta}{\left(\delta_1+\Delta\right)^3\left(\delta_1+2\Delta\right)\left(3\delta_1+2\Delta\right)}, \tag{F4}$$

where Δ is the detuning between the two transmons.

In the experiment, we apply the CR drive and perform Hamiltonian tomography [43] to extract the effective interaction terms emerging from the drive. For a fixed amplitude of the cross-resonance drive we vary the phase of the CR drive and plot the interaction terms as a function of drive phase. The ZZ and IZ terms are independent of the drive phase, whereas the ZX, ZY, IX, and IY terms oscillate periodically [see Fig. 8(a)]. We simultaneously fit the oscillations to sine functions.

We compute Ω, the applied CR drive amplitude from the amplitude of the ZX oscillation, A_{ZX} using Eq. (F3) and plug it to Eq. (F4) to evaluate A_{IX}, the amplitude of IX term arising from CR interaction, in the absence of any crosstalk. Next we measure the phase difference between the ZX and IX oscillations, $\varphi_{\mathrm{CT}} = \varphi_{ZX} - \varphi_{IX}$ and finally compute the crosstalk factor $m = \Omega_{\mathrm{CT}}/\Omega$, where Ω_{CT} is expressed as

$$\Omega_{\mathrm{CT}} = \sqrt{(A_{IX})^2 + 2\cos(\varphi_{\mathrm{CT}})A_{IX}^M A_{IX} + \left(A_{IX}^M\right)^2}, \tag{F5}$$

where A_{IX}^M is the experimentally measured amplitude of the IX oscillations.

We estimate classical crosstalk for four qubit pairs in our system at 30°, 60°, 90°, and 180°. The corresponding values are listed in Table III. The other two pairs are not compatible for a cross-resonance experiment as the pair at 120° has negligible coupling and the pair at 150° has a detuning such that the $(|0\rangle \leftrightarrow |1\rangle)$ transition of the target

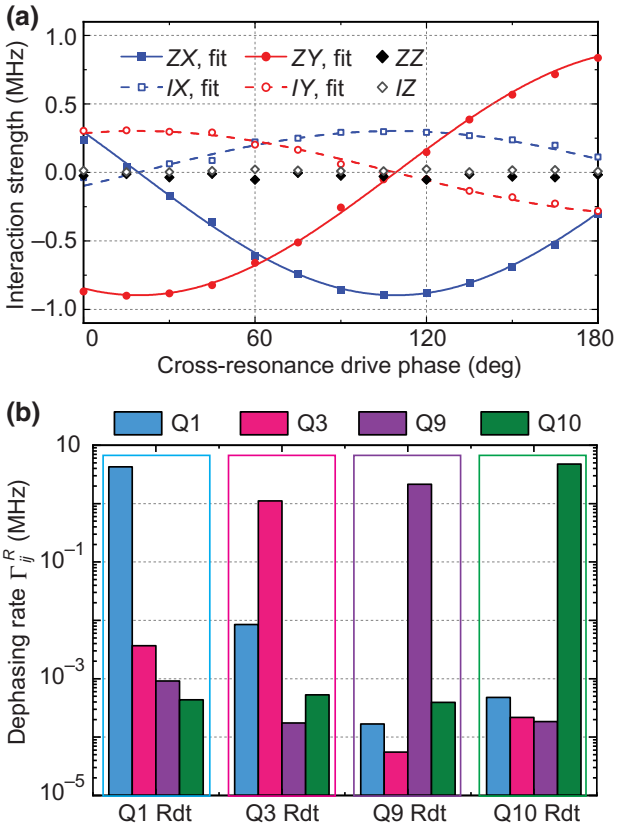

FIG. 8. (a) Characterizing the microwave crosstalk around qubit frequencies. A Hamiltonian tomography experiment is performed under the application of cross resonance drive to quantify the effective interaction terms. The corresponding interaction terms for the pair Q1–Q10 are plotted as a function of the phase of the cross resonance drive applied on Q10. We estimate the classical crosstalk as defined in Eq. (F2) to be $m = 0.1\%$ for this pair. (b) Measurement-induced dephasing rate on the targeted qubit as well as the untargeted qubit due to microwave crosstalk at readout frequencies. Transparent larger box indicates the targeted qubit where we apply the measurement tone whereas the solid boxes refer to the qubit where we perform the echo sequence. We observe a negligible effect on the untargeted qubits measuring at least 3 orders of magnitude lower dephasing rate due to spurious crosstalk except for the Q1–Q3 pair, where the difference is just below 1%.

qubit is resonant with $(|0\rangle \leftrightarrow |2\rangle)/2$ transition of the control qubit. However, we expect the crosstalk to be similar to the other values measured.

Our estimate of crosstalk is in congruence with a previous result [44] showing significantly lower crosstalk in 3D cQED architecture compared to the existing 2D designs [42] due to superior microwave isolation between the cavities. Furthermore, the spatial isolation between qubits in the ring coupler architecture also helps in keeping the crosstalk very low.

TABLE III. Measured classical microwave crosstalk between the cavities around qubit frequencies. CR is not performed between the 120° pair due to negligible coupling and small detuning (< 20 MHz) between the qubits. Also, the pair at 150° has a resonance between the $(|0\rangle \leftrightarrow |1\rangle)$ transition of one qubit and the $(|0\rangle \leftrightarrow |2\rangle)/2$ transition of the other.

CR pair	Q9–Q10	Q1–Q3	Q1–Q10	Q3–Q9
Relative angular positions	30°	60°	90°	180°
CR drive amplitude, Ω (MHz)	28.9	14.7	27.5	21.4
CR crosstalk (m)	0.011	0.008	0.001	0.008

APPENDIX G: READOUT DRIVE CROSSTALK

We characterize the effect of measurement crosstalk on the untargeted qubits while performing readout [45]. To evaluate the effect of microwave crosstalk we perform a Hahn echo experiment and measure the dephasing rate of the untargeted qubit (Q_i) while turning on a continuous calibrated readout tone on the targeted qubit (Q_j). We then compute the excess dephasing rate per photon using the equation:

$$\Gamma_{ij}^R = \frac{1}{\bar{n}}\left(\frac{1}{\tau_i^j} - \frac{1}{\tau_i^0}\right), \tag{G1}$$

where $\bar{n}$ is the average photon number used for the calibrated tone on the targeted qubit. Here τ_i^0 and τ_i^j are Hahn echo times of Q_i with and without the additional tone on Q_j, respectively. We use average photon numbers $\bar{n} = 13$, 19, 11, and 12 for qubits Q1, Q3, Q9, and Q10 to optimize the readout fidelity for each qubit. In Fig. 8(b), we show the effect of crosstalk by plotting the values of Γ_{ij}^R. When compared to the targeted qubit, we observe more than 3 orders of magnitude smaller dephasing rate per photon for the untargeted qubits. The only exception is the Q1–Q3 pair, which has a slightly higher dephasing rate.

[1] Lov K. Grover, in *Proceedings of the Twenty-Eighth Annual ACM Symposium on Theory of Computing* (Association for Computing Machinery, Philadelphia, 1996), p. 212.

[2] Peter W. Shor, Polynomial-time algorithms for prime factorization and discrete logarithms on a quantum computer, SIAM Rev. **41**, 303 (1999).

[3] Petar Jurcevic, Ali Javadi-Abhari, Lev S. Bishop, Isaac Lauer, Daniela F. Bogorin, Markus Brink, Lauren Capelluto, Oktay Günlük, Toshinari Itoko, and Naoki Kanazawa, *et al.*, Demonstration of quantum volume 64 on a superconducting quantum computing system, Quantum Sci. Technol. **6**, 025020 (2021).

[4] Hannes Bernien, Sylvain Schwartz, Alexander Keesling, Harry Levine, Ahmed Omran, Hannes Pichler, Soonwon

Choi, Alexander S. Zibrov, Manuel Endres, and Markus Greiner, *et al.*, Probing many-body dynamics on a 51-atom quantum simulator, Nature **551**, 579 (2017).

[5] Kai Xu, Zheng-Hang Sun, Wuxin Liu, Yu-Ran Zhang, Hekang Li, Hang Dong, Wenhui Ren, Pengfei Zhang, Franco Nori, and Dongning Zheng, *et al.*, Probing dynamical phase transitions with a superconducting quantum simulator, Sci. Adv. **6**, eaba4935 (2020).

[6] Ahmed Omran, Harry Levine, Alexander Keesling, Giulia Semeghini, Tout T. Wang, Sepehr Ebadi, Hannes Bernien, Alexander S. Zibrov, Hannes Pichler, and Soonwon Choi, *et al.*, Generation and manipulation of schrödinger cat states in rydberg atom arrays, Science **365**, 570 (2019).

[7] Frank Arute, Kunal Arya, Ryan Babbush, Dave Bacon, Joseph C. Bardin, Rami Barends, Rupak Biswas, Sergio Boixo, Fernando G. S. L. Brandao, and David A. Buell, *et al.*, Quantum supremacy using a programmable superconducting processor, Nature **574**, 505 (2019).

[8] Tatsuhiro Onodera, Edwin Ng, and Peter L. McMahon, A quantum annealer with fully programmable all-to-all coupling via floquet engineering, npj Quantum Inf. **6**, 1 (2020).

[9] Andrew W. Cross, Lev S. Bishop, Sarah Sheldon, Paul D. Nation, and Jay M. Gambetta, Validating quantum computers using randomized model circuits, Phys. Rev. A **100**, 032328 (2019).

[10] K. Wright, K. M. Beck, S. Debnath, J. M. Amini, Y. Nam, N. Grzesiak, J.-S. Chen, N. C. Pisenti, M. Chmielewski, and C. Collins, *et al.*, Benchmarking an 11-qubit quantum computer, Nat. Commun. **10**, 1 (2019).

[11] Rami Barends, Julian Kelly, Anthony Megrant, Andrzej Veitia, Daniel Sank, Evan Jeffrey, Ted C. White, Josh Mutus, Austin G. Fowler, and Brooks Campbell, *et al.*, Superconducting quantum circuits at the surface code threshold for fault tolerance, Nature **508**, 500 (2014).

[12] Charles Neill, Pedran Roushan, K. Kechedzhi, Sergio Boixo, Sergei V. Isakov, V. Smelyanskiy, A. Megrant, B. Chiaro, A. Dunsworth, and K. Arya, *et al.*, A blueprint for demonstrating quantum supremacy with superconducting qubits, Science **360**, 195 (2018).

[13] J. Majer, J. M. Chow, J. M. Gambetta, Jens Koch, B. R. Johnson, J. A. Schreier, L. Frunzio, D. I. Schuster, Andrew Addison Houck, and Andreas Wallraff, Coupling superconducting qubits via a cavity bus, *et al.*, Nature **449**, 443 (2007).

[14] Chao Song, Kai Xu, Hekang Li, Yu-Ran Zhang, Xu Zhang, Wuxin Liu, Qiujiang Guo, Zhen Wang, Wenhui Ren, and Jie Hao, *et al.*, Generation of multicomponent atomic schrödinger cat states of up to 20 qubits, Science **365**, 574 (2019).

[15] Yu Chen, C. Neill, P. Roushan, N. Leung, M. Fang, R. Barends, J. Kelly, B. Campbell, Z. Chen, B. Chiaro, A. Dunsworth, E. Jeffrey, A. Megrant, J. Y. Mutus, P. J. J. O'Malley, C. M. Quintana, D. Sank, A. Vainsencher, J. Wenner, T. C. White, Michael R. Geller, A. N. Cleland, and John M. Martinis, Qubit Architecture with High Coherence and Fast Tunable Coupling, Phys. Rev. Lett. **113**, 220502 (2014).

[16] David C. McKay, Ravi Naik, Philip Reinhold, Lev S. Bishop, and David I. Schuster, High-Contrast Qubit Interactions Using Multimode Cavity qed, Phys. Rev. Lett. **114**, 080501 (2015).

[17] M. A. Rol, F. Battistel, F. K. Malinowski, C. C. Bultink, B. M. Tarasinski, R. Vollmer, N. Haider, N. Muthusubramanian, A. Bruno, B. M. Terhal, and L. DiCarlo, Fast, High-Fidelity Conditional-Phase Gate Exploiting Leakage Interference in Weakly Anharmonic Superconducting Qubits, Phys. Rev. Lett. **123**, 120502 (2019).

[18] S. A. Caldwell, N. Didier, C. A. Ryan, E. A. Sete, A. Hudson, P. Karalekas, R. Manenti, M. P. da Silva, R. Sinclair, and E. Acala, *et al.*, Parametrically Activated Entangling Gates Using Transmon Qubits, Phys. Rev. Appl. **10**, 034050 (2018).

[19] Chad Rigetti and Michel Devoret, Fully microwave-tunable universal gates in superconducting qubits with linear couplings and fixed transition frequencies, Phys. Rev. B **81**, 134507 (2010).

[20] S. Krinner, P. Kurpiers, B. Royer, P. Magnard, I. Tsitsilin, J.-C. Besse, A. Remm, A. Blais, and A. Wallraff, Demonstration of an All-Microwave Controlled-Phase Gate between Far-Detuned Qubits, Phys. Rev. Appl. **14**, 044039 (2020).

[21] Felix Borjans, X. G. Croot, Xiao Mi, M. J. Gullans, and J. R. Petta, Resonant microwave-mediated interactions between distant electron spins, Nature **577**, 195 (2020).

[22] Peng-Chao Xu, J. W. Rao, Y. S. Gui, Xiaofeng Jin, and C.-M. Hu, Cavity-mediated dissipative coupling of distant magnetic moments: Theory and experiment, Phys. Rev. B **100**, 094415 (2019).

[23] Andrey B. Matsko and Vladimir S. Ilchenko, Optical resonators with whispering-gallery modes-part I: Basics, IEEE J. Sel. Top. Quantum. Electron. **12**, 3 (2006).

[24] Z. K. Minev, I. M. Pop, and M. H. Devoret, Planar superconducting whispering gallery mode resonators, Appl. Phys. Lett. **103**, 142604 (2013).

[25] Wenhui Huang, Yuxuan Zhou, Ziyu Tao, Libo Zhang, Song Liu, Yuanzhen Chen, Tongxing Yan, and Dapeng Yu, A superconducting coplanar waveguide ring resonator as quantum bus for circuit quantum electrodynamics, Appl. Phys. Lett. **118**, 184001 (2021).

[26] Anton Frisk Kockum, Per Delsing, and Göran Johansson, Designing frequency-dependent relaxation rates and lamb shifts for a giant artificial atom, Phys. Rev. A **90**, 013837 (2014).

[27] Bharath Kannan, Max J. Ruckriegel, Daniel L. Campbell, Anton Frisk Kockum, Jochen Braumüller, David K. Kim, Morten Kjaergaard, Philip Krantz, Alexander Melville, and Bethany M. Niedzielski, *et al.*, Waveguide quantum electrodynamics with superconducting artificial giant atoms, Nature **583**, 775 (2020).

[28] Jens Koch, Terri M. Yu, Jay Gambetta, A. A. Houck, D. I. Schuster, J. Majer, Alexandre Blais, M. H. Devoret, S. M. Girvin, and R. J. Schoelkopf, Charge-insensitive qubit design derived from the cooper pair box, Phys. Rev. A **76**, 042319 (2007).

[29] Firat Solgun, David W. Abraham, and David P. DiVincenzo, Blackbox quantization of superconducting circuits using exact impedance synthesis, Phys. Rev. B **90**, 134504 (2014).

[30] Simon E. Nigg, Hanhee Paik, Brian Vlastakis, Gerhard Kirchmair, S. Shankar, Luigi Frunzio, M. H. Devoret, R. J.

Schoelkopf, and S. M. Girvin, Black-Box Superconducting Circuit Quantization, Phys. Rev. Lett. **108**, 240502 (2012).

[31] Hanhee Paik, D. I. Schuster, Lev S. Bishop, G. Kirchmair, G. Catelani, A. P. Sears, B. R. Johnson, M. J. Reagor, L. Frunzio, L. I. Glazman, S. M. Girvin, M. H. Devoret, and R. J. Schoelkopf, Observation of High Coherence in Josephson Junction Qubits Measured in a Three-Dimensional Circuit qed Architecture, Phys. Rev. Lett. **107**, 240501 (2011).

[32] J. Z. Blumoff, K. Chou, C. Shen, M. Reagor, C. Axline, R. T. Brierley, M. P. Silveri, C. Wang, B. Vlastakis, S. E. Nigg, L. Frunzio, M. H. Devoret, L. Jiang, S. M. Girvin, and R. J. Schoelkopf, Implementing and Characterizing Precise Multiqubit Measurements, Phys. Rev. X **6**, 031041 (2016).

[33] Gerhard Kirchmair, Brian Vlastakis, Zaki Leghtas, Simon E. Nigg, Hanhee Paik, Eran Ginossar, Mazyar Mirrahimi, Luigi Frunzio, Steven M. Girvin, and Robert J. Schoelkopf, Observation of quantum state collapse and revival due to the single-photon kerr effect, Nature **495**, 205 (2013).

[34] See Supplemental Material at http://link.aps.org/supplemental/10.1103/PhysRevApplied.16.024018 for additional data.

[35] Youpeng Zhong, Hung-Shen Chang, Audrey Bienfait, Étienne Dumur, Ming-Han Chou, Christopher R. Conner, Joel Grebel, Rhys G. Povey, Haoxiong Yan, and David I. Schuster, *et al.*, Deterministic multi-qubit entanglement in a quantum network, Nature **590**, 571 (2021).

[36] Fei Yan, Simon Gustavsson, Archana Kamal, Jeffrey Birenbaum, Adam P. Sears, David Hover, Ted J. Gudmundsen, Danna Rosenberg, Gabriel Samach, and Steven Weber, *et al.*, The flux qubit revisited to enhance coherence and reproducibility, Nat. Commun. **7**, 1 (2016).

[37] Long B. Nguyen, Yen-Hsiang Lin, Aaron Somoroff, Raymond Mencia, Nicholas Grabon, and Vladimir E. Manucharyan, High-Coherence Fluxonium Qubit, Phys. Rev. X **9**, 041041 (2019).

[38] I. M. Georgescu, S. Ashhab, and Franco Nori, Quantum simulation, Rev. Mod. Phys. **86**, 153 (2014).

[39] Earl T. Campbell, Barbara M. Terhal, and Christophe Vuillot, Roads towards fault-tolerant universal quantum computation, Nature **549**, 172 (2017).

[40] David M. Pozar, *Microwave Engineering* (Wiley, Hoboken, NJ, 2005), 3rd ed..

[41] Jerry M. Chow, A. D. Córcoles, Jay M. Gambetta, Chad Rigetti, B. R. Johnson, John A. Smolin, J. R. Rozen, George A. Keefe, Mary B. Rothwell, Mark B. Ketchen, and M. Steffen, Simple All-Microwave Entangling Gate for Fixed-Frequency Superconducting Qubits, Phys. Rev. Lett. **107**, 080502 (2011).

[42] Easwar Magesan and Jay M. Gambetta, Effective hamiltonian models of the cross-resonance gate, Phys. Rev. A **101**, 052308 (2020).

[43] Sarah Sheldon, Easwar Magesan, Jerry M. Chow, and Jay M. Gambetta, Procedure for systematically tuning up cross-talk in the cross-resonance gate, Phys. Rev. A **93**, 060302 (2016).

[44] Sumeru Hazra, Kishor V. Salunkhe, Anirban Bhattacharjee, Gaurav Bothara, Suman Kundu, Tanay Roy, Meghan P. Patankar, and R. Vijay, Engineering cross resonance interaction in multi-modal quantum circuits, Appl. Phys. Lett. **116**, 152601 (2020).

[45] Johannes Heinsoo, Christian Kraglund Andersen, Ants Remm, Sebastian Krinner, Theodore Walter, Yves Salathé, Simone Gasparinetti, Jean-Claude Besse, Anton Potočnik, Andreas Wallraff, and Christopher Eichler, Rapid High-Fidelity Multiplexed Readout of Superconducting Qubits, Phys. Rev. Appl. **10**, 034040 (2018).